



Catalytic reactions of dioxygen with ethane and methane on platinum clusters: Mechanistic connections, site requirements, and consequences of chemisorbed oxygen

Mónica García-Diéguez^a, Ya-Huei (Cathy) Chin^a, Enrique Iglesia^{a,b,*}

^a Department of Chemical Engineering, University of California at Berkeley, Berkeley, CA 94720, USA

^b Division of Chemical Sciences, E.O. Lawrence Berkeley National Laboratory, Berkeley, CA 94720, USA

ARTICLE INFO

Article history:

Received 10 July 2011

Revised 17 September 2011

Accepted 27 September 2011

Available online 17 November 2011

Keywords:

CH₄ oxidation

C₂H₆ oxidation

Combustion

Platinum

C–H bond activation

Oxygen reactivity

Alkane oxidation

ABSTRACT

C₂H₆ reactions with O₂ only form CO₂ and H₂O on dispersed Pt clusters at 0.2–28 O₂/C₂H₆ reactant ratios and 723–913 K without detectable formation of partial oxidation products. Kinetic and isotopic data, measured under conditions of strict kinetic control, show that CH₄ and C₂H₆ reactions involve similar elementary steps and kinetic regimes. These kinetic regimes exhibit different rate equations, kinetic isotope effects and structure sensitivity, and transitions among regimes are dictated by the prevalent coverages of chemisorbed oxygen (O*). At O₂/C₂H₆ ratios that lead to O*-saturated surfaces, kinetically-relevant C–H bond activation steps involve O*–O* pairs and transition states with radical-like alkyls. As oxygen vacancies (*) emerge with decreasing O₂/alkane ratios, alkyl groups at transition states are effectively stabilized by vacancy sites and C–H bond activation occurs preferentially at O*–* site pairs. Measured kinetic isotope effects and the catalytic consequences of Pt cluster size are consistent with a monotonic transition in the kinetically-relevant step from C–H bond activation on O*–O* site pairs, to C–H bond activation on O*–* site pairs, to O₂ dissociation on *–* site pairs as O* coverage decrease for both C₂H₆ and CH₄ reactants. When C–H bond activation limits rates, turnover rates increase with increasing Pt cluster size for both alkanes because coordinatively unsaturated corner and edge atoms prevalent in small clusters lead to more strongly-bound and less-reactive O* species and lower densities of vacancy sites at nearly saturated cluster surfaces. In contrast, the highly exothermic and barrierless nature of O₂ activation steps on uncovered clusters leads to similar turnover rates on Pt clusters with 1.8–8.5 nm diameter when this step becomes kinetically-relevant at low O₂/alkane ratios. Turnover rates and the O₂/alkane ratios required for transitions among kinetic regimes differ significantly between CH₄ and C₂H₆ reactants, because of the different C–H bond energies, strength of alkyl–O* interactions, and O₂ consumption stoichiometries for these two molecules. Vacancies emerge at higher O₂/alkane ratios for C₂H₆ than for CH₄ reactants, because their weaker C–H bonds lead to faster scavenging of O* and to lower O* coverages, which are set by the kinetic coupling between C–H and O=O activation steps. The elementary steps, kinetic regimes, and mechanistic analogies reported here for C₂H₆ and CH₄ reactions with O₂ are consistent with all rate and isotopic data, with their differences in C–H bond energies and in alkyl binding, and with the catalytic consequences of surface coordination and cluster size. The rigorous mechanistic interpretation of these seemingly complex kinetic data and cluster size effects provides useful kinetic guidance for larger alkanes and other catalytic surfaces based on the thermodynamic properties of these molecules and on the effects of metal identity and surface coordination on oxygen binding and reactivity.

© 2011 Elsevier Inc. All rights reserved.

1. Introduction

Catalytic conversion of light alkanes (CH₄ [1–6], C₂H₆ [7–10]) via oxidative routes enables the use of natural gas in the generation of synthesis gas and power and in the removal of volatile organic

* Corresponding author at: Department of Chemical Engineering, University of California at Berkeley, Berkeley, CA 94720, USA. Fax: +1 510 642 4778.

E-mail address: iglesia@berkeley.edu (E. Iglesia).

compounds from combustion effluents. CH₄–O₂ reactions on Pt- [11,12], Rh- [12], and Pd- [13] supported clusters form only CO₂ and H₂O at all practical inlet O₂/CH₄ ratios under conditions of strict kinetic control. ¹²CO–¹³CH₄–O₂ reactions on Pd [13] and Pt [12] and DFT-derived barriers for CO and CH₄ reactions with chemisorbed oxygen (O*) on Pt clusters are consistent with CO as the preferential scavenger of O*. These data also confirm that direct catalytic partial oxidation routes, which would convert CH₄–O₂ reactants directly to H₂–CO mixtures, does not occur at practical

conditions or conversions. Any CO* that desorbs before subsequent oxidation would readsorb and form CO₂ at any residence time required for practical CH₄ conversions [12,13].

On Pt, CH₄–O₂ reaction rates are described by three kinetic regimes when O₂ is present and an additional (reforming) regime when H₂O or CO₂ are used as the oxidants to scavenge CH₄-derived surface intermediates [11]. Each regime exhibits distinct rate equations and effects of metal cluster size, which reflect the involvement of different elementary steps and most abundant surface intermediates (MASI), the nature of which is consistent with observed kinetic effects of reactants and products on rates and with isotopic exchange rates and kinetic isotope effects [11].

Larger alkanes react faster than CH₄ [14,15] because of their weaker C–H bonds; their elementary steps and their kinetic relevance may well resemble those involved in CH₄ reactions [11], but interpretations of the rates of larger alkanes in terms of the identity and kinetic relevance of elementary steps and any mechanistic connections among alkanes of different size have remained speculative and controversial [7–10]. The oxidation of C₂H₆ is even more exothermic than for CH₄ ($\Delta H_{298}^0 = -1428.5 \text{ kJ (mol C}_2\text{H}_6\text{)}^{-1}$; $\Delta H_{298}^0 = -802.6 \text{ kJ (mol CH}_4\text{)}^{-1}$ [16]); these enthalpies can lead to ubiquitous and severe local temperature and concentration gradients, which corrupt the intended kinetic origins of rate and selectivity data. Here, we report mechanistic analogies between CH₄ and C₂H₆ reactions with O₂ and predictive models of their relative rates and kinetic response to reactant concentrations. The conclusions reached and the mechanistic interpretations proposed are based on kinetic and isotopic data measured under conditions of strict kinetic control, which required extents of catalyst dilution by inert solids much greater than in any previous studies.

We find that CH₄ and C₂H₆ oxidation proceed via identical elementary steps and exhibit similar kinetic regimes on Pt clusters. These regimes and their respective rate equations and cluster size effects are similar for the two reactants, but turnover rates and the O₂/C_nH_{2n+2} (*n* = 1, 2) ratios that define the transitions among these regimes differ because the reactivity of C–H bonds in CH₄ and C₂H₆ differ significantly. These kinetic regimes respond to a monotonic evolution in O* coverage from saturated to uncovered surfaces as O₂/C_nH_{2n+2} ratios decrease and to a concomitant shift from O*–O* to O*– site pairs as the active sites for C–H bond dissociation and to the ultimate evolution of O₂ activation as the sole kinetically-relevant step as O* coverages become very small. O* coverages depend on C–H bond reactivity and strength because of the prevalent kinetic coupling between C–H and O=O activation steps. These mechanistic conclusions seem relevant to larger alkanes and to other catalytic metals, as recently shown for CH₄–O₂ [13] and CH₄–H₂O/CO₂ [17,18] reactions on Pd and Rh clusters.

2. Experimental methods

2.1. Catalyst synthesis

Pt/ γ -Al₂O₃ catalysts were prepared by incipient wetness impregnation of the support (γ -Al₂O₃, Sasol North America Inc., lot no. C1643, 193 m² g⁻¹, 0.57 cm³ g⁻¹) with an aqueous solution of hexachloroplatinic acid (H₂PtCl₆(H₂O)₆, Aldrich, CAS #16941-12-1) to obtain a Pt weight loading of 0.2%. γ -Al₂O₃ was treated in flowing dry air (Praxair, 99.99%, 0.8 cm³ g⁻¹ s⁻¹) before impregnation by heating to 923 K at 0.083 K s⁻¹ and holding for 3 h. Impregnated samples were kept in ambient air at 383 K for 8 h, then treated in flowing dry air (Praxair, 99.99%, 0.8 cm³ g⁻¹ s⁻¹) to 823 K for 3 h, and separated into three portions; each portion was treated at different temperatures between 900 K and 1023 K in flowing dry air (Praxair, 99.99%, 0.8 cm³ g⁻¹ s⁻¹) for 5 h to vary Pt dispersion and cluster size. The samples were then brought to ambient temperature in flowing dry air, flushed with He, and then treated at 873–923 K in

flowing H₂ (10% in Ar, Praxair certified standard, 0.083 K s⁻¹, 0.8 cm³ g⁻¹ s⁻¹) for 2 h. Samples were cooled to ambient temperature in He (Praxair UHP grade) and passivated by contact with 1% O₂–He flow (Praxair certified standard, 0.8 cm³ g⁻¹ s⁻¹) for 4 h. Pt dispersions (Pt_{surface}/Pt_{total}) were measured from volumetric uptakes of strongly-chemisorbed H₂ at 313 K (Quantasorb Chemisorption Analyzer; Quantachrome Corp.) by extrapolating isotherms to zero H₂ pressures. Mean cluster diameters were estimated from dispersion values assuming hemispherical clusters and clusters with the bulk density of Pt metal (21.5 g cm⁻³; [19]).

2.2. Turnover rate and selectivity measurements

Steady-state C₂H₆ and CH₄ turnover rates were measured at 723–913 K using a fritted quartz tube (8.1 mm inner diameter) equipped with a concentric quartz thermowell that held a K-type thermocouple. Catalysts (0.2 % wt. Pt/Al₂O₃) were diluted with inert SiO₂ (Grace–Davison, chromatographic silica media, CAS no. 112926-00-8, 280 m² g⁻¹) to form mixtures with SiO₂/catalyst intraparticle mass ratios (λ) of 100–300 (weight basis) and pelleted and sieved to retain 100–250- μ m aggregates. These aggregates were then diluted with acid-washed quartz granules (100–250 μ m, Fluka, #84880) at quartz/catalyst mass ratios (χ) of 1400–11,700. SiO₂ (Grace–Davison) and acid-washed quartz were treated in dry air (Praxair, 99.99%, 0.8 cm³ g⁻¹ s⁻¹) at 1123 K (0.083 K s⁻¹) for 5 h and at 1173 K (0.083 K s⁻¹) for 2 h, respectively, before forming these mixtures. Neither SiO₂ nor quartz granules gave detectable reaction rates at any of the conditions of catalytic experiments.

Reactants were metered electronically (Porter, type 201 mass flow controllers) by mixing 10% C₂H₆/He (Praxair certified standard), 25% CH₄/He (Praxair certified standard), 5% O₂/He (Praxair certified standard), 1% O₂/He (Praxair certified standard), O₂ (Praxair UHP grade), and He (Praxair UHP grade). Doubly-distilled deionized H₂O was introduced using a microsyringe pump (Cole Parmer, Model 60061; Hamilton #1001 syringe) into the reactant gases at 423 K, and all lines were kept above 400 K to prevent condensation.

Catalysts were treated in 5% H₂/He (Praxair UHP grade; 1.67 cm³ s⁻¹) by heating to 773 K at 0.083 K s⁻¹ and holding for 600 s. He was introduced (Praxair UHP grade; 1.67 cm³ s⁻¹) for 600 s before contacting samples with reactants. Reactant and product concentrations were measured by gas chromatography using an Agilent 3000A Micro GC, Poraplot Q or Mol Sieve 5A columns and thermal conductivity detection.

2.3. Isotopic exchange and kinetic effects

¹⁶O₂–¹⁸O₂ exchange rates and C–H/C–D kinetic isotope effects were measured using the reactors and protocols described above. C₂D₆ (Isotec, 99 atom% D) and 5% ¹⁸O₂/He (Isotec, 97 atom% ¹⁸O) were used in C₂D₆–¹⁶O₂, C₂H₆–¹⁶O₂–¹⁸O₂ and ¹⁶O₂–¹⁸O₂ mixtures. The concentrations of different oxygen isotopologues (¹⁶O₂, ¹⁶O¹⁸O, ¹⁸O₂) and of C₂D₆ were measured using a mass-selective detector (Agilent 5973) and a gas chromatograph (Agilent 3000A Micro GC), respectively. Samples were exposed to C₂H₆–¹⁶O₂–¹⁸O₂ mixtures for 0.5 h to ensure isotopic equilibration between dioxygen and lattice oxygen atoms before acquiring oxygen exchange rate data [11].

3. Results and discussion

3.1. Detection and removal of mass and heat transport corruptions

C₂H₆–O₂ reactions gave CO₂ and H₂O and only trace amounts of CO or H₂ on all Pt catalysts (1.8–8.5 nm mean cluster diameter,

723–913 K) and at all O₂ and C₂H₆ pressures (0.04–28 O₂/C₂H₆), as also observed for CH₄–O₂ reactions on Pt, Rh, and Pd over a broader temperature range [11–13]. Trace CO concentrations (CO/CO₂ = 0.007–0.01) were detected only at effluent O₂/C₂H₆ ratios below 0.2 (CO/CO₂ ratios vs. O₂ or C₂H₆ pressure in Supplementary information, Section S1). These C₂H₆ combustion reactions are fast and very exothermic ($\Delta H_{298}^0 = -1428.5 \text{ kJ (mol C}_2\text{H}_6)^{-1}$ [16]), and severe exotherms and intrapellet gradients prevail in the absence of extensive dilution within aggregates (intrapellet) and packed beds (interparticle), which decreases the volumetric rates of reactant depletion and heat release [20,21]. Turnover rates that are unaffected by further dilution represent the only unequivocal demonstration of strict kinetic control.

The effects of dilution at the pellet ($\lambda = 200$ –1000) and bed ($\chi = 1400$ –11,700) scales on C₂H₆–O₂ turnover rates ($r_{\text{C}_2\text{H}_6}$) were measured on 0.2 % wt. Pt/Al₂O₃ (8.5 nm clusters) at 773 K (1 kPa C₂H₆, 0.1–4.0 kPa O₂; Fig. 1, Table 1). At O₂ pressures below ~0.8 kPa, turnover rates did not depend on dilution ratios (Fig. 1); these constant rates are not resulted from concentration gradients of O₂ but instead rates that exhibit very low activation barriers in this kinetic regime and therefore depend only weakly on local temperatures (Section 3.5). At O₂ pressures above 0.8 kPa, C₂H₆ turnover rates were higher at λ values of 200 than for values above 300 at all O₂ pressures (Fig. 1, Table 1, $\chi = 7000$), indicating that intraparticle dilution ratios larger than 300 are sufficient and essential for kinetic control (for these bed dilution ratios and reactor diameters).

The bed dilution ratios required for isothermal conditions were probed by varying χ from 1400 to ~12,000 at pellet dilution ratios of 300–1000 (Fig. 1, Table 1). Bed dilution ratios of 1400 led to higher C₂H₆ turnover rates than those obtained with χ values larger than 7000, for which C₂H₆ turnover rates became independent of the bed dilution (Table 1). These data show that λ and χ values larger than 300 and 7000, respectively, lead to local concentrations and temperatures identical to those in the fluid phase in which they are experimentally measured; therefore, the measured turnover rates for such diluted catalysts rigorously reflect the kinetic response of Pt clusters to temperature and concentrations, even at the highest rates reported in Fig. 1. Intraparticle (λ) and interparticle (χ) dilution ratios of 300 and 7000, respectively, correspond to $8 \times 10^{-3} \text{ W cm}^{-3}$ volumetric heat release rates, which can be removed from these tubular reactions (8.1 mm diameter) without kinetically-detectable axial or radial gradients. We note that these

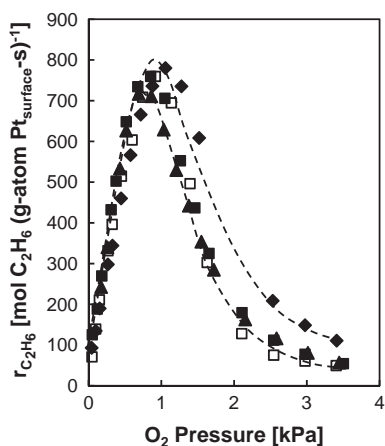


Fig. 1. Effects of intraparticle and interparticle dilution ratios on ethane turnover rates ($r_{\text{C}_2\text{H}_6}$) on 0.2 % wt. Pt/Al₂O₃ (8.5 nm mean cluster diameter). (773 K; intraparticle SiO₂/catalyst dilution ratios (λ) of 200 (◆), 300 (■, □) and 1000 (▲); interparticle quartz/catalyst dilution ratios (χ) of 7000 (◇, ▲) and 11,700 (□); $6.0 \times 10^7 \text{ cm}^3$ (STP) $\text{g}^{-1} \text{ h}^{-1}$; 1 kPa C₂H₆.)

dilution requirements are several orders of magnitude larger than in any previous combustion studies, some of which report rate data of purported kinetic origins. These dilution requirements must be strictly met for measured rates and selectivities to reflect their intended chemical origins [20,21], as is the case for all C₂H₆–O₂ conversion turnover rates reported in the present study.

3.2. Kinetic dependence of ethane turnover rates on C₂H₆ and O₂ pressures

Fig. 2a and b shows the effects of O₂ (0.1–45 kPa) and C₂H₆ (0.5–2.5 kPa) pressures on ethane conversion turnover rates (0.2 % wt. Pt/Al₂O₃, 8.5 nm clusters; 773 K). These diverse kinetic responses are denoted as kinetic regimes 1–3, by analogy with notation used to describe similar kinetic trends for CH₄–O₂ reactions on Pt [11]. H₂O (5 kPa) added to inlet C₂H₆–O₂ mixtures (Fig. 2a and b) did not influence rates in any of these kinetic regimes. We conclude that H₂O does not compete for active sites at these conditions and that C₂H₆–H₂O reforming reactions do not occur at detectable rates during C₂H₆–O₂ reactions at conditions that do not deplete O₂ co-reactants.

Fig. 3a and b shows pseudo-first-order rate constants (turnover rates divided by alkane pressure, $r_{\text{C}_n\text{H}_{2n+2}} (\text{C}_n\text{H}_{2n+2})^{-1}$) for C₂H₆ and CH₄ reactions with O₂ on Pt/Al₂O₃ (0.2 % wt. Pt, 8.5 nm) as a function of oxidant/reductant ratios (O₂/C_nH_{2n+2}) at 773 K. Pseudo-first-order rate constants for each reactant were observed to behave as single-valued functions of the respective (O₂/C_nH_{2n+2}) ratios, as also shown for CH₄–O₂ reactions at higher temperatures (773–900 K) on Pt clusters [11]. CH₄ and C₂H₆ reactants show analogous transitions among kinetic regimes and similar dependences on O₂/C_nH_{2n+2} ratios within each regime, but turnover rates are much higher and the transitions between regimes occur at larger O₂/C_nH_{2n+2} ratios for C₂H₆ than CH₄ reactants. These differences reflect C–H bond energies that are much lower in C₂H₆ than CH₄ and kinetically-relevant steps and most abundant adsorbed species that are similar for these two reactants (as discussed in detail in Sections 3.3–3.6).

Pseudo-first-order rate constants were not affected by O₂/C_nH_{2n+2} ratios at high reactant ratios (regime 1, O₂/C₂H₆ > 8; O₂/CH₄ > 0.35), which lead to O*–saturated cluster surfaces (Section 3.3). Rate constants increased with decreasing O₂/C_nH_{2n+2} ratios (regime 2) because lower O* coverages led to the appearance of vacant sites (*), which activate C–H bonds much more effectively than O*–O* site pairs (Section 3.4). At very low O₂/C_nH_{2n+2} ratios (regime 3, O₂/C₂H₆ < 0.7; O₂/CH₄ < 0.03) clusters become essentially uncovered, O₂ dissociation is the sole kinetically-relevant step, and rate constants become proportional to O₂/C_nH_{2n+2} rates, consistent with turnover rates that depend linearly on O₂ pressures but are insensitive to the pressure (and identity) of alkane co-reactants (Section 3.5).

Table 1

Effects of intraparticle (λ) and interparticle (χ) dilution ratios on ethane turnover rates measured on 0.2 % wt. Pt/Al₂O₃ (8.5 nm mean Pt cluster diameter; 100–250 μm catalyst pellet diameters and 8.1 mm reactor bed diameter) at 773 K.

Intraparticle dilution ratio (λ)	Interparticle dilution ratio (χ)	Turnover rate ^a (mol C ₂ H ₆ (g-atom Pt _{surface} -s) ⁻¹)	Heat release rate ($\times 10^3 \text{ W cm}^{-3}$)
200	7000	110	30
300	1400	109	57
300	7000	49	8
300	11,700	54	7
500	7000	44	9
500	11,700	48	7
700	11,700	50	7

^a $6.0 \times 10^7 \text{ cm}^3$ (STP) $\text{g}^{-1} \text{ h}^{-1}$; 1 kPa C₂H₆; 3.5 kPa O₂.

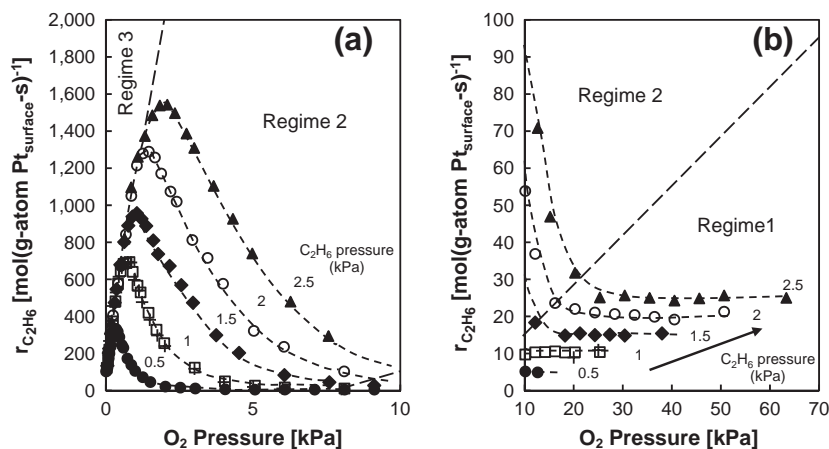


Fig. 2. (a and b) Ethane turnover rates ($r_{\text{C}_2\text{H}_6}$) as a function of O_2 pressure, in the range of (a) 0–10 kPa and (b) 10–70 kPa of O_2 , on 0.2% wt. Pt/ Al_2O_3 (8.5 nm mean cluster diameter) during C_2H_6 – O_2 reactions with 0.5 kPa (●), 1 kPa (□), 1.5 kPa (◆), 2 kPa (○) and 2.5 kPa (▲) of C_2H_6 and C_2H_6 – O_2 – H_2O reactions (+) with 1 kPa of C_2H_6 and 5 kPa of H_2O . (773 K; intraparticle SiO_2 /catalyst ratio (λ) of 300; interparticle quartz/catalyst ratio (χ) of 7000; $6.0 \times 10^7 \text{ cm}^3$ (STP) $\text{g}^{-1} \text{ h}^{-1}$).

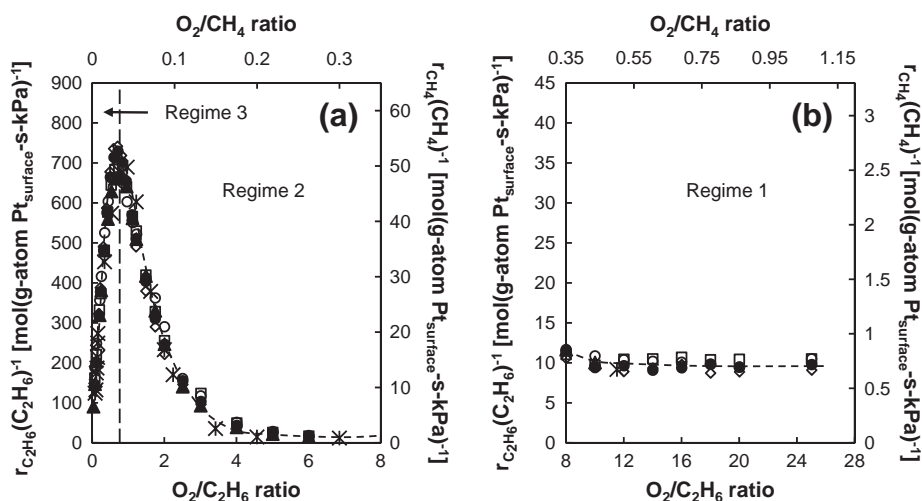


Fig. 3. (a and b) Pseudo-first-order rate constants ($r_{\text{C}_n\text{H}_{2n+2}}(\text{C}_n\text{H}_{2n+2})^{-1}$) during C_2H_6 – O_2 reactions with 0.25 kPa (◇), 0.5 kPa (●), 1 kPa (□), 1.5 kPa (◆), 2 kPa (○) and 2.5 kPa (▲) of C_2H_6 and during CH_4 – O_2 reactions with 4.9 kPa (✕) of CH_4 on 0.2% wt. Pt/ Al_2O_3 (8.5 nm mean cluster diameter). (a) Regime 2: $\text{O}_2/\text{C}_2\text{H}_6 = 0.7$ – 8 , $\text{O}_2/\text{CH}_4 = 0.03$ – 0.35 and regime 3: $\text{O}_2/\text{C}_2\text{H}_6 = 0$ – 0.7 , $\text{O}_2/\text{CH}_4 = 0$ – 0.03 ; (b) regime 1: $\text{O}_2/\text{C}_2\text{H}_6 > 8$, $\text{O}_2/\text{CH}_4 > 0.35$. (773 K; intraparticle SiO_2 /catalyst ratio (λ) of 300; interparticle quartz/catalyst ratio (χ) of 7000; $6.0 \times 10^7 \text{ cm}^3$ (STP) $\text{g}^{-1} \text{ h}^{-1}$).

The $\text{O}_2/\text{C}_n\text{H}_{2n+2}$ ratios that cause transitions between kinetic regimes are larger by a factor of 23 (± 4) for C_2H_6 – O_2 than CH_4 – O_2 reactions, as shown by the data in Fig. 3a and b, in which the abscissas shown for these two alkane reactants differ by this factor (of 23). Similarly, first-order rate constants for C_2H_6 are larger than for CH_4 by a factor of 13 (± 2) when $\text{O}_2/\text{C}_2\text{H}_6$ ratios are offset by the 23-fold abscissa factor, as shown by the respective ordinates used in Fig. 3a and b for the two alkane reactants. The coincidence of these C_2H_6 and CH_4 rate data when adjusted in this manner (Fig. 3a and b) suggests that differences in C–H bond strength and reactivity cause the observed differences in turnover rates and also in the reactant ratios required to achieve the O^* coverages that cause transitions between kinetic regimes.

The sequence of elementary steps in Scheme 1 and their kinetic relevance are examined next to provide a rigorous description of these kinetic phenomena and also a mechanistic basis for the analogous behavior of alkanes of different size and C–H bond strength. In Scheme 1, O_2 adsorbs molecularly and then dissociates on vacancy sites ($*$) (steps 2.a and 2.b). These steps are coupled kinetically with the activation of C–H bonds in $\text{C}_n\text{H}_{2n+2}$ reactants by

O^*-O^* or O^*-* site pairs (steps 1.1–1.2, Scheme 1), depending on the O^* coverage and the concomitant availability of vacant sites. The remaining steps complete the catalytic turnovers by forming H_2O , CO_2 , CO , and H_2 products (steps 3–10, Scheme 1). The kinetically-relevant step and the most abundant surface intermediates must shift as O^* coverages and $\text{O}_2/\text{C}_n\text{H}_{2n+2}$ ratios decrease in order to account for the diverse kinetic effects shown in Figs. 2a and b and 3a and b. In what follows, we report kinetic and isotopic evidence for the relevance and reversibility of these steps in each kinetic regime, starting with kinetic regime 1, in which clusters are saturated with O^* and C–H bond activation on O^*-O^* site pairs is the sole kinetically-relevant step for both CH_4 and C_2H_6 reactants.

3.3. C_2H_6 – O_2 reactions on Pt sites saturated with chemisorbed oxygen: kinetic regime 1

Pseudo-first-order rate constants for C_2H_6 – O_2 reactions ($r_{\text{C}_2\text{H}_6}(\text{C}_2\text{H}_6)^{-1}$) at 773 K were not affected by $\text{O}_2/\text{C}_2\text{H}_6$ ratios when these ratios were larger than 8. CH_4 – O_2 reactions behaved

Table 2Kinetically-relevant step, rate equation, effective rate constant, and C–H/C–D kinetic isotope effects in each kinetic regime during C₂H₆–O₂, CH₄–O₂, and C₂D₆–O₂ reactions on Pt clusters.

	Kinetically-relevant steps Rate equation Effective rate constant	Effective rate constants ($k_{\text{effX-CnH}}$) at 773 K [mol C _n H _{2n+2} (g-atom Pt _{surface} -s-kPa) ⁻¹] ^a		KIE _X ^b ($\frac{r_{\text{C}_2\text{H}_6}}{r_{\text{C}_2\text{D}_6}}$)
		$k_{\text{effX-C2H}}$	$\left(\frac{k_{\text{effX-C2H}}}{k_{\text{effX-CH}}}\right)$	
Regime 1	$\text{C}_n\text{H}_{2n+2} + \text{O}^* + \text{O}^* \xrightarrow{k_{1,1-\text{CnH}}} \text{C}_n\text{H}_{2n+1}\text{O}^* + \text{OH}^*$ $r_{\text{C}_n\text{H}_{2n+2}} = k_{\text{eff1-CnH}}(\text{C}_n\text{H}_{2n+2})$ $k_{\text{eff1-CnH}} = K_{1,1-\text{CnH}}$	9.6 ± 0.7	14 ± 2	1.9 ± 0.3
Regime 2	$\text{C}_n\text{H}_{2n+2} + \text{O}^* + \text{O}^* \xrightarrow{k_{1,2-\text{CnH}}} \text{C}_n\text{H}_{2n+1}\text{O}^* + \text{OH}^*$ $\text{O}_2 + 2^* \xrightarrow{K_{2a}K_{2b}} 2\text{O}^*$ $r_{\text{C}_n\text{H}_{2n+2}} = k_{\text{eff2-CnH}} \frac{(\text{C}_n\text{H}_{2n+2})^2}{(\text{O}_2)}$ $k_{\text{eff2-CnH}} = \left(\frac{3n+1}{2}\right) \frac{K_{1,2-\text{CnH}}^2}{K_{2a}K_{2b}}$	710 ± 30	280 ± 70	7.8 ± 0.8 ^c
Regime 3	$\text{O}_2 + 2^* \xrightarrow{K_{2a}K_{2b}} 2\text{O}^*$ $r_{\text{C}_n\text{H}_{2n+2}} = k_{\text{eff3-CnH}}(\text{O}_2)$ $k_{\text{eff3-CnH}} = \left(\frac{2}{3n+1}\right) K_{2a}K_{2b}$	1590 ± 20	0.57 ± 0.02	0.98 ± 0.08

 $n = 1$ for CH₄, 2 for C₂H₆; X = regime 1, 2 or 3.^a Effective rate constants at 773 K on 0.2 wt. Pt/Al₂O₃ (8.5 nm mean cluster diameter) during C₂H₆–O₂ ($k_{\text{effX-C2H}}$) and CH₄–O₂ ($k_{\text{effX-CH}}$) reactions.^b C–H/C–D kinetic isotope effects ($r_{\text{C}_2\text{H}_6}/r_{\text{C}_2\text{D}_6}$) at 773 K.^c Calculated from Eq. (6), the effective rate constants for C₂H₆ and C₂D₆ were determined by least-square regression of $r_{\text{C}_2\text{H}_6}(\text{C}_2\text{H}_6)^{-1}$ vs. C₂H₆/O₂ (or $r_{\text{C}_2\text{D}_6}(\text{C}_2\text{D}_6)^{-1}$ vs. C₂D₆/O₂) data.

and C₂H₆ combustion reactions. When surfaces are saturated with O* ($(\text{O}^*) \gg (*)$), Eq. (2) becomes identical to Eq. (1), irrespective of whether O₂ dissociation is equilibrated ($k_{1,1-\text{CnH}}(\text{C}_n\text{H}_{2n+2}) \ll k_{2\text{br}}$) or irreversible ($k_{1,1-\text{CnH}}(\text{C}_n\text{H}_{2n+2}) \gg k_{2\text{br}}$).

The reversibility of O₂ activation steps (step 2.b) can be independently probed by comparing ¹⁶O¹⁸O isotopologue formation rates from C₂H₆–¹⁶O₂–¹⁸O₂ and ¹⁶O₂–¹⁸O₂ mixtures. ¹⁶O¹⁸O formation rates are proportional to O* coverages [11,23], and quasi-equilibrated O₂ dissociation would give high and similar exchange rates in the presence and absence of alkane co-reactants. In ¹⁶O₂–¹⁸O₂ mixtures, O₂ activation steps are chemically equilibrated and O*–to-* ratios depend only on O₂ pressures according to the equation:

$$\left(\frac{\text{O}^*}{(*)}\right)_{\text{eq}} = \sqrt{K_{2a}K_{2b}(\text{O}_2)} \quad (3)$$

in which the subscript eq denotes chemical equilibrium and K_{2a} and K_{2b} are the equilibrium constants for molecular O₂ adsorption (step 2.a, Scheme 1) and dissociation (step 2.b, Scheme 1), respectively. The ratio of ¹⁶O₂–¹⁸O₂ isotopic exchange rates in C₂H₆–¹⁶O₂–¹⁸O₂ ($r_{\text{ex,ss}}$; ss denotes steady-state) and ¹⁶O₂–¹⁸O₂ ($r_{\text{ex,eq}}$) mixtures at a given O₂ pressure is defined as η and reflects the extent of O* equilibration with O₂(g) during C₂H₆–¹⁶O₂–¹⁸O₂ reactions [11]:

$$\eta = \frac{r_{\text{ex,ss}}}{r_{\text{ex,eq}}}\bigg|_{\text{O}_2\text{pressure}} = \frac{f((\text{O}^*)_{\text{ss}})}{f((\text{O}^*)_{\text{eq}})} \quad (4)$$

Values of η near unity indicate that O* coverages during C₂H₆–O₂ catalysis are unaffected by the reductant or its oxidation reactions, which scavenge O* species, and that O* coverages reflect solely their equilibration with O₂(g). These η values were measured from isotopic exchange rates with and without C₂H₆ (0.5 kPa; 0.2 wt. Pt/Al₂O₃, 8.5 nm clusters, 773 K) for a range of O₂/C₂H₆ reactant ratios in each kinetic regime (Fig. 4). Values of η were near unity in kinetic regime 1, indicating that O₂ dissociation is quasi-equilibrated, that O* coverages are a single-valued function of O₂ pressure, and that the insensitivity of C₂H₆–O₂ turnover rates to O₂ concentrations in regime 1 reflects the presence of saturated O* monolayers in equilibrium with O₂(g). As O₂/C₂H₆ ratios decrease (to values smaller than 8), η concurrently decreases (Fig. 4), indicating that higher C₂H₆ pressures prevent O₂ dissociation equilibrium by rapidly scavenging O* before their recombi-

tion and desorption as O₂(g) (consistent with the $k_{1,1-\text{CnH}}(\text{C}_n\text{H}_{2n+2}) \ll k_{2\text{br}}$ inequality required for equilibration of step 2). The increase in pseudo-first-order rate constants ($r_{\text{C}_n\text{H}_{2n+2}}(\text{C}_n\text{H}_{2n+2})^{-1}$) at low O₂/C₂H₆ ratios (<8) also suggests the emergence of O*–* site pairs, which lead to more effective C–H bond activation routes than those provided by O*–O* site pairs, as we show here for C₂H₆–O₂ reactions and elsewhere for CH₄–O₂ reactions on Pt [11] and Pd [13] clusters.

3.4. C₂H₆–O₂ reactions on O*–* site pairs: kinetic regime 2

Pseudo-first-order rate constants for C₂H₆–O₂ reactions ($r_{\text{C}_2\text{H}_6}(\text{C}_2\text{H}_6)^{-1}$) increased as O₂/C₂H₆ ratios decreased from 8 to 0.7, at which point they reached a maximum value (Fig. 3a; 773 K) and then decreased; these trends are also evident for CH₄–O₂ reactions at 773 K (Fig. 3a) and 873 K [11], but maximum rates are achieved at O₂/C₂H₆ ratios ~23 times smaller for CH₄ than for C₂H₆ at 773 K.

The rate data in regime 2 and the kinetic consequences of O₂/C₂H₆ reactant ratios (Fig. 3a) are described by a rate equation

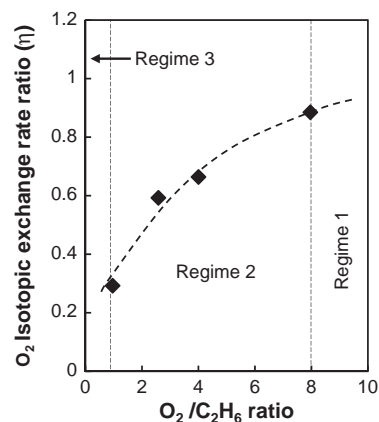


Fig. 4. Ratio of ¹⁶O₂–¹⁸O₂ isotopic exchange rates in C₂H₆–¹⁶O₂–¹⁸O₂ ($r_{\text{ex,ss}}$) and ¹⁶O₂–¹⁸O₂ ($r_{\text{ex,eq}}$) mixtures ($\eta = r_{\text{ex,ss}}/r_{\text{ex,eq}}$) as a function of O₂/C₂H₆ ratio on 0.2 wt. Pt/Al₂O₃ (773 K; 8.5 nm mean Pt cluster diameter). (0.5 kPa C₂H₆; ss: steady state; eq: equilibrium; reaction conditions as described in Fig. 3a and b.)

derived from C–H bond activation on O*–* site pairs (step 1.2) and its kinetic coupling with irreversible O₂ dissociation steps (step 2.b) to establish pseudo-steady-state concentrations for all adsorbed species in Scheme 1 and O* as the prevalent MASI (derivation in Supplementary information, Section S3):

$$\frac{r_{C_nH_{2n+2}}}{(C_nH_{2n+2})} = k_{1.2-CnH} \left(\frac{\left(\frac{3n+1}{2}\right) k_{1.2-CnH} (C_nH_{2n+2})}{K_{2a} k_{2bf} (O_2)} \right) = k_{\text{eff}2-CnH} \frac{(C_nH_{2n+2})}{(O_2)} \quad (5)$$

(a) (b)

In this equation, $k_{1.2-CnH}$ ($k_{1.2-C_2H_6}$ for C₂H₆, $k_{1.2-C_1H}$ for CH₄) and k_{2bf} are the rate constants for C–H bond activation (on O*–* pairs) and O₂ dissociation, respectively (as defined in Scheme 1). The effective rate constants defined by Eq. (5) ($k_{\text{eff}2-CnH}$) are shown in Table 2 for both C₂H₆ and CH₄ reactants (0.2 % wt. Pt/Al₂O₃, 8.5 nm clusters; 773 K). The $\left(\frac{3n+1}{2}\right)$ term in Eq. (5) represents the O₂ consumption stoichiometry per alkane molecule (3.5 for C₂H₆; 2 for CH₄), K_{2a} is the equilibrium constant for molecular O₂ adsorption, and k_{2bf} is the rate constant for O₂ dissociation. This equation for the effective first-order rate constants in regime 2 reflects the product of the reactive collision probabilities of alkanes with cluster surfaces (term labeled (a) in Eq. (5)) and the fraction of the cluster surfaces containing vacant sites at O* coverages near saturation levels (term labeled (b) in Eq. (5)).

Eq. (5) accurately describes the observed inverse dependence of effective first-order CH₄ and C₂H₆ oxidation rate constants on O₂/C_nH_{2n+2} ratios in this kinetic regime (O₂/C₂H₆ = 0.7–8; O₂/CH₄ = 0.03–0.35; Fig. 3a). These rate constants are proportional to C_nH_{2n+2}/O₂ ratios (C₂H₆/O₂ = 0.125–1.4; CH₄/O₂ = 2.9–33), and $k_{\text{eff}2-C_2H_6}$ in Eq. (5) is given by the slope in the C₂H₆–O₂ rate data shown in Fig. 5. At high C_nH_{2n+2}/O₂ ratios (C₂H₆/O₂ = 1–1.4; CH₄/O₂ = 25–33), the rate constants depart slightly from the linear trend with C_nH_{2n+2}/O₂ ratios predicted by Eq. (5); the mechanistic implications for these slight deviations are discussed below and reflect changes in rate constants for C–H and O=O activation with O* coverage.

The irreversible nature of O₂ dissociation and the concomitant deviations of O* coverages from their equilibrium values were confirmed from ¹⁶O₂–¹⁸O₂ exchange rates with C₂H₆–¹⁶O₂–¹⁸O₂ and in ¹⁶O₂–¹⁸O₂ mixtures. In this regime, the rate ratios of oxygen isotopologue formation in C₂H₆–¹⁶O₂–¹⁸O₂ and ¹⁶O₂–¹⁸O₂ mixtures (η) were smaller than unity and decreased with decreasing O₂/C₂H₆ reactant ratios (Fig. 4). These trends reflect the more effective activation of C–H bonds on O*–* compared with O*–O* pairs, which leads to the more effective scavenging of O* species via reactions with C₂H₆.

The rate constants for C₂D₆–O₂ and C₂H₆–O₂ reactions are shown in Fig. 5 as a function of the respective C₂D₆/O₂ and C₂H₆/O₂ ratios. The measured rate constants for C₂H₆–O₂ ($k_{\text{eff}2-C_2H_6}$) and C₂D₆–O₂ ($k_{\text{eff}2-C_2D_6}$) reactions (from the slopes of rate data in Fig. 5) are $710 \pm 30 \text{ kPa}^{-1} \text{ s}^{-1}$ and $91 \pm 3 \text{ kPa}^{-1} \text{ s}^{-1}$, respectively (Table 2; 773 K). Their ratio provides the C–H/C–D kinetic isotope effects in kinetic regime 2 (KIE₂) for a given reductant/oxidant reactant ratio:

$$\text{KIE}_2 = \frac{\left(\frac{r_{C_2H_6}}{C_2H_6}\right)}{\left(\frac{r_{C_2D_6}}{C_2D_6}\right)} = \left(\frac{k_{1.2-C_2H_6}}{k_{1.2-C_2D_6}}\right)^2 \left(\frac{\left(\frac{2}{3n+1}\right) K_{2a} k_{2bf} (C_2H_6)}{\left(\frac{2}{3n+1}\right) K_{2a} k_{2bf} (C_2D_6)}\right) \frac{(C_2H_6)}{(C_2D_6)} \frac{(O_2)}{(O_2)}$$

$$= \frac{k_{\text{eff}2-C_2H_6}}{k_{\text{eff}2-C_2D_6}} \frac{(C_2H_6)}{(C_2D_6)} \frac{(O_2)}{(O_2)} \quad (6)$$

In this equation, K_{2a} and k_{2bf} are the O₂ adsorption equilibrium constant and O₂* dissociation rate constant, respectively (Scheme 1) and $k_{1.2-C_2H_6}$ (or $k_{1.2-C_2D_6}$) is the C–H (or C–D) bond dissociation rate constant on O*–* site pairs. The O₂ adsorption

equilibrium constant (K_{2a}) and the O₂* dissociation rate constant (k_{2bf}) do not depend on the isotopic identity of the reductant (C₂H₆ or C₂D₆); thus, measured C–H/C–D kinetic isotope effects for a given reductant/oxidant reactant ratio merely reflect the ratio of the C–H to C–D bond activation rate constants to the second power:

$$\text{KIE}_2 = \left(\frac{k_{1.2-C_2H_6}}{k_{1.2-C_2D_6}}\right)^2 \frac{(C_2H_6)}{(C_2D_6)} \frac{(O_2)}{(O_2)} \quad (7)$$

These values reflect the value of these two rate constants at the prevalent O* and * coverages, which differ for C₂H₆ and C₂D₆ reactants because of their different reactivity and effectiveness in reactions with O*. Measured C–H/C–D kinetic isotope effects (7.8 ± 0.3 ; 773 K, Table 2) indicate that C–H bond activation is indeed a kinetically-relevant step in this regime; these KIE₂ values, however, are larger than expected from the square of the C–H/C–D kinetic isotope effects measured on O*–O* site pairs in regime 1 (Table 2, $(k_{1.1-C_2H_6}/k_{1.1-C_2D_6})^2 \sim 3.6$). These larger KIE₂ values and the slight deviations from the expected linear dependence on reductant/oxidant ratio at high C₂H₆/O₂ ratios (Fig. 5) reflect rate constants for both C–H and O=O activation that vary slightly with O* coverage, as vicinal vacancies emerge with decreasing O* coverage. At these intermediate O* coverages, lateral interactions between O* species cause the reactivity and binding properties of O*–* pairs to vary with O* coverage, as shown by DFT calculations of C–H bond activation barriers on O* covered Pt clusters [11]. As a result, Langmuirian kinetic treatments and Eq. (5) become approximate and rates and kinetic isotope effects must then be measured for C₂H₆ and C₂D₆ reactants at the same O* coverages, as shown below; these KIE values for C₂H₆–O₂ and C₂D₆–O₂ reactants at similar O* coverages are denoted here as KIE_{2,O*}.

Steady-state O* coverages during C₂H₆–O₂ (and C₂D₆–O₂) reactions ($(O^*)/(^*)_{\text{SS,H}}$ and $(O^*)/(^*)_{\text{SS,D}}$) in regime 2 are set by the O₂/C₂H₆ (or O₂/C₂D₆) ratios according to:

$$\frac{(O^*)}{(^*)}_{\text{SS,H or D}} = \left(\frac{2}{3n+1}\right) \frac{K_{2a} k_{2bf}}{k_{1.2-CnH}} \frac{(O_2)}{(C_nH_{2n+2} \text{ or } C_nD_{2n+2})} \quad (8)$$

This equation is derived from the kinetic coupling of the irreversible C–H (or C–D) and O=O bond activation steps that determine such O* coverages (steps 1.2 and 2.b, Scheme 1; Supplementary information, Section S3). The rate and equilibrium constants in Eq. (8) correspond to the steps in Scheme 1. At the same O* coverage, the

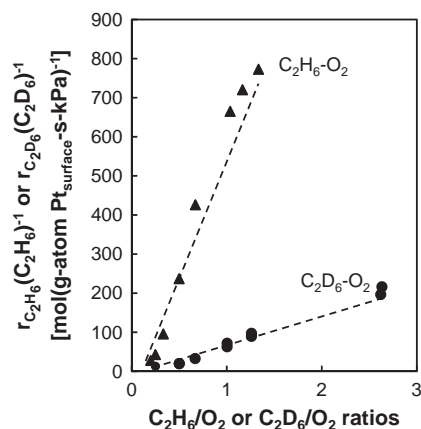


Fig. 5. Pseudo-first-order rate constants ($r_{C_2H_6}/(C_2H_6)^{-1}$ and $r_{C_2D_6}/(C_2D_6)^{-1}$) during C₂H₆–O₂ (▲) and C₂D₆–O₂ (●) reactions in kinetic regime 2 (O₂/C₂H₆ = 0.7–8) as a function of C₂H₆/O₂ or C₂D₆/O₂ ratios on 0.2 % wt. Pt/Al₂O₃ (8.5 nm mean cluster diameter). (1 kPa C₂H₆ or C₂D₆; reaction conditions as described in Fig. 3a and b.)

right-hand side of this equation is the same for $C_2H_6-O_2$ and $C_2D_6-O_2$ reactions and gives:

$$\left(\frac{2}{7}\right) \frac{K_{2a}k_{2bf}}{k_{1.2-C_2H}} \frac{(O_2)}{(C_2H_6)} = \left(\frac{2}{7}\right) \frac{K_{2a}k_{2bf}}{k_{1.2-C_2D}} \frac{(O_2)}{(C_2D_6)} \quad (9)$$

This equation gives the C_2D_6/O_2 and C_2H_6/O_2 ratios that give rise to the same O^* coverage in terms of the ratio of C–H bond activation rate constants for deuterated and undeuterated reactants:

$$\frac{\left(\frac{C_2H_6}{O_2}\right)_{|O^*}}{\left(\frac{C_2D_6}{O_2}\right)_{|O^*}} = \frac{k_{1.2-C_2D}}{k_{1.2-C_2H}} \quad (10)$$

Substituting Eq. (10) into Eq. (7) leads to C–H/C–D kinetic isotope effects at the same O^* coverage for C_2H_6 and C_2D_6 reactants (KIE_{2,O^*}):

$$KIE_{2,O^*} = \frac{\left(\frac{r_{C_2H_6}}{C_2H_6}\right)}{\left(\frac{r_{C_2D_6}}{C_2D_6}\right)} \Big|_{O^*} = \frac{k_{1.2-C_2H}}{k_{1.2-C_2D}} \Big|_{O^*} \quad (11)$$

which requires that these rates be measured for these two reactants at their respective reactant ratios that give the same O^* coverage and which correspond to different reactant ratios. For any given C_2H_6/O_2 ratio, which sets the O^* coverage and the corresponding pseudo-first-order rate constant ($r_{C_2H_6}(C_2H_6)^{-1}$) (Fig. 5), the kinetic isotope effects at the same O^* coverage can then be obtained using a recursive method. An initial estimate for the rate constant ratio ($(k_{1.2-C_2H}/k_{1.2-C_2D})_{|O^*}$) gives a value for the C_2D_6/O_2 ratio for the same O^* coverages as for $C_2H_6-O_2$ reactions (Eq. (10)). The pseudo-first-order rate constant in $C_2D_6-O_2$ reactions ($r_{C_2D_6}(C_2D_6)^{-1}$) at this C_2D_6/O_2 ratio is then estimated by interpolation of the rate data in Fig. 5. This process is repeated for a new estimate of the rate constant ratio ($(k_{1.2-C_2H}/k_{1.2-C_2D})_{|O^*}$) until it becomes equal to the measured ratio ($(r_{C_2H_6}/C_2H_6)/(r_{C_2D_6}/C_2D_6)_{|O^*}$, Eq. (11)) (Supplementary information, Section S4 shows a sample calculation in more detail).

These KIE_{2,O^*} values are shown in Table 3 for several C_2H_6/O_2 ratios, used here as the experimental surrogate for O^* coverage. Kinetic isotope effects at O^* coverages near saturation ($C_2H_6/O_2 = 0.125$, $KIE_{2,O^*} = 1.9$) are consistent with the kinetic relevance of C–H bond activation steps; they are similar to those measured for C–H and C–D bond activation steps on O^*-O^* site pairs in regime 1 ($KIE_1 = k_H/k_D = 1.9$, Table 2, Section 3.3). As C_2H_6/O_2 ratios increase and oxygen vacancies become more abundant, KIE_{2,O^*} values increased gradually from 1.9 to 2.8 (Table 3) and the apparent C–H bond activation rate constant increased concurrently (Fig. 5). These changes in KIE_{2,O^*} values with O^* coverages reflect concomitant changes in the antisymmetric vibrations that constitutes the reaction coordinate. DFT treatments of C–H bond activation on O^*-O^* site pairs show that surface Pt atoms insert into C–H bonds and H abstraction is assisted by vicinal O^* atoms [11]. Lateral interactions among O^* species weaken and Pt–O bonds strengthen with decreasing O^* coverage, rendering O^* species less reactive in H abstraction. The d-electron density in Pt atoms increases [24] and Pt–C and Pt–H bonds become stronger with decreasing O^* coverages [11,12] and transition states exhibit shorter C–H bonds and longer O–H bonds [11] and occur earlier along the reaction coordinate. Maximum KIE values are typically found at intermediate stages along the reaction coordinate, while exothermic steps with early transition states and endothermic steps with late transition states give smaller values [25]. The symmetric stretch along the reaction coordinate for thermoneutral steps has the same frequency for H and D reactants at their respective transition states; as a result, activation barriers for C–H and C–D bond differ only by their ground-state energies (18–19 kJ mol⁻¹ and 12 kJ mol⁻¹ for C_2H_6 and C_2D_6 , respectively [26,27]) and give maximum KIE values (k_H/k_D) of 2.5–3.0 at 773 K (according to the second

approximation proposed by Westheimer [25]). Thus, KIE_{2,O^*} values that increase gradually as vacancies become more abundant (from 1.9 to 2.8, Table 3) till reaching KIE values similar to those expected from nearly symmetric transition-state structures near the midpoint along the reaction coordinate are consistent with transition states that occur earlier along the reaction coordinate as the fraction of vacancy sites increases.

3.5. $C_2H_6-O_2$ reactions limited by O_2 dissociation on bare surfaces: kinetic regime 3

Pseudo-first-order rate constants ($k_{\text{eff}3-C_{nH}}$) for C_2H_6 and CH_4 reactions with O_2 :

$$\frac{r_{C_nH_{2n+2}}}{(C_nH_{2n+2})} = k_{\text{eff}3-C_{nH}} \frac{(O_2)}{(C_nH_{2n+2})} \quad (12)$$

decreased linearly with increasing O_2/C_nH_{2n+2} ratios for ratios smaller than 0.03 and 0.7 for CH_4 and C_2H_6 , respectively (773 K, Fig. 3a; Pt/Al₂O₃, 0.2 % wt. Pt, 8.5 nm clusters). In this regime, turnover rates become proportional to O_2 pressures but are unaffected by the concentration or identity of the reductant (Fig. 2a). These data indicate that O_2 dissociation (Step 2.b, Scheme 1) on bare Pt surfaces (*, MASI) limits turnover rates in kinetic regime 3 for both CH_4 and C_2H_6 reactions with O_2 .

O_2 consumption rates are identical for $C_2H_6-O_2$, $C_2D_6-O_2$, and CH_4-O_2 reactions at 773 K within experimental accuracy (Fig. 6), indicating that C–H bond activation steps (and therefore C–H bond energies) become kinetically-irrelevant at these low O^* coverages and that there are no detectable C–H/C–D kinetic isotope effects ($(r_{C-H}/r_{C-D}) = 0.98 \pm 0.08$, Table 2). The value of $k_{\text{eff}3-C_{nH}}$ in Eq. (12) represents the reactive collision probability of O_2 with Pt cluster surfaces and reflects the product of the equilibrium constant for molecular O_2 adsorption (K_{2a}) and the O_2 dissociation rate constant (k_{2bf}) (steps 2.a and 2.b in Scheme 1, respectively):

$$k_{\text{eff}3-C_{nH}} = \left(\frac{2}{3n+1}\right) K_{2a}k_{2bf} \quad (13)$$

in which the $((3n+1)/2)$ is the ratio of the stoichiometric O_2 requirements for CO_2 and H_2O formation per C_nH_{2n+2} alkane.

The $K_{2a}k_{2bf}$ values determined from $C_2H_6-O_2$ and CH_4-O_2 reactions at 773 K are $5.56 \times 10^3 \text{ kPa}^{-1} \text{ s}^{-1}$ (C_2H_6) and $5.58 \times 10^3 \text{ kPa}^{-1} \text{ s}^{-1}$ (CH_4) (Table 2) and correspond to O_2 sticking coefficients of $\sim 10^{-2}$, which resemble those measured from O_2 dissociation rates on Pt(111) surfaces (0.1 at 673 K [28]; 0.05 at 658 K [29]). These high reactive probabilities reflect the essentially barrierless nature of O_2 dissociation steps, as also observed for CH_4-O_2 reactions on bare Pt cluster surfaces (3 kJ mol⁻¹) and estimated from DFT (20 kJ mol⁻¹) on uncovered Pt₂₀₁ clusters [11]. These low activation barriers also lead to the similar rates at 773 K and 873 K for both C_2H_6 and CH_4 reactants (Fig. 6).

The irreversible nature of O_2 dissociation steps, inferred from their sole kinetic relevance in $C_2H_6-O_2$ reactions on nearly bare surfaces within this kinetic regime, was confirmed from the ratios of ¹⁶O¹⁸O formation from $C_2H_6-^{18}O_2-^{16}O_2$ and $^{18}O_2-^{16}O_2$ mixtures (η). The η values at these low O_2/C_2H_6 ratios ($O_2/C_2H_6 < 0.7$) were much smaller than unity and also much smaller than those measured in regime 2 (Fig. 4); they show that O_2 dissociation steps are essentially irreversible and that O^* coverages are indeed very low at the O_2/C_2H_6 ratios that define the kinetic regime 3.

3.6. Mechanistic connections between $C_2H_6-O_2$ and CH_4-O_2 reactions on Pt clusters

The evidence presented here clearly show that $C_2H_6-O_2$ and CH_4-O_2 reactions proceed via similar kinetic regimes and

Table 3C–H/C–D kinetic isotope effects in kinetic regime 2 determined from ethane turnover rates at equal O* coverage ($\text{KIE}_{2,0^*}$) at 773 K on Pt clusters.

In $\text{C}_2\text{H}_6\text{--O}_2$		In $\text{C}_2\text{D}_6\text{--O}_2$ at equal O* coverage that in $\text{C}_2\text{H}_6\text{--O}_2$		$\text{KIE}_{2,0^*}^d$
$\text{C}_2\text{H}_6/\text{O}_2^a$	$r_{\text{C}_2\text{H}_6}(\text{C}_2\text{H}_6)^{-1}$ (mol C_2H_6 (g-atom $\text{Pt}_{\text{surface-s-kPa}})^{-1}$)	$\text{C}_2\text{D}_6/\text{O}_2^b$	$r_{\text{C}_2\text{H}_6}(\text{C}_2\text{D}_6)^{-1c}$ (mol C_2D_6 (g-atom $\text{Pt}_{\text{surface-s-kPa}})^{-1}$)	
0.125	15	0.24	8	1.9
0.2	28	0.4	14	2.0
0.25	43	0.53	20	2.1
0.35	96	0.8	42	2.3
0.5	240	1.25	95	2.5
0.6	340	1.6	130	2.6
0.7	426	1.9	160	2.7
1	660	2.8	230	2.8

^a $\text{C}_2\text{H}_6/\text{O}_2$ ratios, used here as experimental surrogate for O* coverage (Eq. (8)).^b $\text{C}_2\text{D}_6/\text{O}_2$ calculated for equal O* coverages that those set by $\text{C}_2\text{H}_6/\text{O}_2$ ratios in $\text{C}_2\text{H}_6\text{--O}_2$ mixtures (Eq. (10)).^c Interpolated from Fig. 5.^d Calculated as the ratio $\left(\frac{r_{\text{C}_2\text{H}_6}}{r_{\text{C}_2\text{D}_6}}\right)_{\text{O}^*}$ (see Supplementary information, Section S4 for an example of the calculations).

sequences of elementary steps, but with transitions among regimes that depend on the reactivity of the reductant. These transitions reflect the effectiveness of these two reactants in scavenging O*, which determines in turn (i) O* coverages; (ii) the identity and kinetic involvement of the most abundant surface intermediates (MASI); and (iii) the fraction of exposed Pt atoms available for binding the C-atom in the activated C–H bond. Here, we explore in more detail the mechanistic basis and relations for the different C–H bond activation rate constants and for the $\text{O}_2/\text{C}_n\text{H}_{2n+2}$ ratios required for the kinetic transitions observed in CH_4 and C_2H_6 reactions with O_2 (Fig. 3a and b).

The pseudo-first-order rate constants for $\text{C}_2\text{H}_6\text{--O}_2$ reactions in regime 1 ($\text{O}_2/\text{C}_2\text{H}_6 > 8$) represent the true rate constants for C–H bond activation on $\text{O}^*\text{--O}^*$ site pairs. Their values are 14 ± 2 times ($k_{1.1\text{-C}_2\text{H}_6}/k_{1.1\text{-C}_1\text{H}_4}$, Table 2) larger than for $\text{CH}_4\text{--O}_2$ reactions ($\text{O}_2/\text{CH}_4 > 0.35$) (0.2 % wt. Pt/ Al_2O_3 ; 8.5 nm clusters; 773 K, Fig. 3). Rate constants for C–H bond activation in C_2H_6 on $\text{O}^*\text{--O}^*$ site pairs are shown in Fig. 7 in the form suggested by the Arrhenius equation, together with the corresponding rate constants for $\text{CH}_4\text{--O}_2$ reactions in regime 1 [11]. Activation barriers for C–H bond activation in C_2H_6 (110 ± 10 kJ mol⁻¹) are significantly smaller than for CH_4 (155 ± 9 kJ mol⁻¹). Pre-exponential factors for the C_2H_6 activation step (2.0×10^8 kPa⁻¹ s⁻¹) are ~10 times smaller than for CH_4 activation steps (2.1×10^9 kPa⁻¹ s⁻¹) [11]. These pre-exponential values are higher than for transition states with full two-dimensional translation ($\sim 1 \times 10^4$ kPa⁻¹ s⁻¹), indicating that these transition-state structures retain most of the entropy of the gaseous alkane reactants. DFT treatments of C–H bond activation steps (in CH_4) on O*-saturated Pt clusters [11] and extended Pt [11] and Pd [30] surfaces have shown that H abstraction by O* involves the formation of radical-like CH_3 groups at the transition state; these radical-like species interact only very weakly with vicinal O* species. The large pre-exponential factors reported here for $\text{C}_2\text{H}_6\text{--O}_2$ reactions are consistent with the involvement of similar high-entropy ethyl radicals at the transition states required for C–H bond activation in C_2H_6 .

The measured differences in C–H bond activation barriers for CH_4 and C_2H_6 reactants (45 kJ mol⁻¹) are actually larger than the differences in their respective C–H bond dissociation energies (440 ± 1 kJ mol⁻¹ CH_4 , 423 ± 2 kJ mol⁻¹ C_2H_6 [31]). DFT calculations have shown that O–H bonds are nearly formed at transition states for C–H bond activation [11], indicating that stronger interactions of ethyl radicals with surfaces must account for $\text{C}_2\text{H}_6\text{--O}_2$ barriers that differ from those for $\text{CH}_4\text{--O}_2$ by more than their respective C–H bond energies. These interactions must involve the incipient coordination of C_2H_5 species to O* at cluster surfaces, because van der Waals energies increase with alkane chain size by only 5–6.5 kJ mol⁻¹ per C-atom [32]; therefore, the additional

5–6.5 kJ mol⁻¹ for C_2H_6 cannot fully account for the 28 kJ mol⁻¹ additional difference in barriers between $\text{CH}_4\text{--O}_2$ and $\text{C}_2\text{H}_6\text{--O}_2$ (45 kJ mol⁻¹) beyond the corresponding C–H bond energies (17 kJ mol⁻¹). Indeed, the entropy loss upon formation of the transition state (from measured pre-exponential factors) is higher for C_2H_6 (37 J mol⁻¹ K⁻¹) than for CH_4 (18 J mol⁻¹ K⁻¹, [11]), consistent with C_2H_5 fragments that are less mobile than CH_3 fragments and more strongly bound to O* species at the transition state. Alkyl–O interactions increase with alkyl size in alkoxides derived from alkanols on metals, for which the C–O bond strength in alkoxides correlates with that in the corresponding gas-phase alkanol [33,34]. The stronger incipient binding of ethyls relative to methyls on O*-covered surfaces is consistent with these trends (C–O bond strengths of 334.9 kJ mol⁻¹ in CH_3OH and 347.1 kJ mol⁻¹ in $\text{C}_2\text{H}_5\text{OH}$ [35]).

In regime 2, pseudo-first-order rate constants for $\text{C}_2\text{H}_6\text{--O}_2$ reactions (regime 2; $\text{O}_2/\text{C}_2\text{H}_6 = 0.7\text{--}8$) are larger than for $\text{CH}_4\text{--O}_2$ reactions ($\text{O}_2/\text{CH}_4 = 0.03\text{--}0.35$) (Fig. 3a). At each $\text{O}_2/\text{C}_n\text{H}_{2n+2}$ ratio, rate constants for C_2H_6 are ~280 times larger than for CH_4 ($k_{\text{eff}2\text{-C}_2\text{H}_6}/k_{\text{eff}2\text{-C}_1\text{H}_4}$, Table 2). At the $\text{O}_2/\text{C}_n\text{H}_{2n+2}$ ratios leading to maximum rates, which reflect a transition from O* to * as MASI, rate constants for C_2H_6 (at $\text{O}_2/\text{C}_2\text{H}_6 = 0.7$) are ~15 times higher than for CH_4 (at $\text{O}_2/\text{CH}_4 = 0.03$). The intermediate O* coverages required for this transition occur at $\text{O}_2/\text{C}_n\text{H}_{2n+2}$ ratios ~23 times larger for C_2H_6 than CH_4 (Fig. 3a), because of the higher reactivity of C–H bonds in C_2H_6 . O* coverages during $\text{CH}_4\text{--O}_2$ and $\text{C}_2\text{H}_6\text{--O}_2$ reactions in regime 2 are set by the prevalent $\text{O}_2/\text{C}_n\text{H}_{2n+2}$ ratios and given by Eq. (8) (Section 3.4). At the same O* coverage, the right-hand side of Eq. (8) becomes the same for $\text{C}_2\text{H}_6\text{--O}_2$ and $\text{CH}_4\text{--O}_2$ reactants and gives:

$$\left(\frac{2}{7}\right) \frac{K_{2a}k_{2\text{bf}}(\text{O}_2)}{k_{1.2\text{-C}_2\text{H}_6}} = \left(\frac{2}{4}\right) \frac{K_{2a}k_{2\text{bf}}(\text{O}_2)}{k_{1.2\text{-C}_1\text{H}_4}} \quad (14)$$

This equation relates the $\text{O}_2/\text{C}_2\text{H}_6$ ratios (for $\text{C}_2\text{H}_6\text{--O}_2$ reactions) and O_2/CH_4 ratios (for $\text{CH}_4\text{--O}_2$ reactions) required to achieve the same O* coverage through the ratio of C–H bond activation rate constants for the two reactants on $\text{O}^*\text{--O}^*$ site pairs ($k_{1.2\text{-C}_2\text{H}_6}/k_{1.2\text{-C}_1\text{H}_4}$) and the O_2 consumption stoichiometry for C_2H_6 (3.5) and CH_4 (2.0) reactions (derivation in Supplementary information, Section S5):

$$\left(\frac{\text{O}_2}{\text{C}_2\text{H}_6}\right)_{\text{O}^*} = \left(\frac{3.5}{2}\right) \frac{k_{1.2\text{-C}_2\text{H}_6}}{k_{1.2\text{-C}_1\text{H}_4}} \left(\frac{\text{O}_2}{\text{CH}_4}\right)_{\text{O}^*} \quad (15)$$

The ratio of C–H bond activation rate constants in regime 2 ($\sqrt{(2/3.5)k_{\text{eff}2\text{-C}_2\text{H}_6}/k_{\text{eff}2\text{-C}_1\text{H}_4}}$; Table 2; Supplementary information, Section S5) equals 13 ± 2 (Table 2) on Pt surfaces (8.5 nm mean cluster size, 773 K). This ratio leads to $\text{O}_2/\text{C}_2\text{H}_6$ ratios in $\text{C}_2\text{H}_6\text{--O}_2$

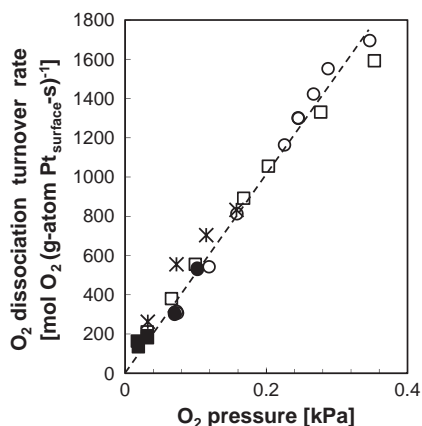


Fig. 6. Oxygen dissociation turnover rates in kinetic regime 3 during $C_2H_6-O_2$ (\square), $C_2D_6-O_2$ (\blacksquare), and CH_4-O_2 (\times) reactions at 773 K, CH_4-O_2 (\circ) and CD_4-O_2 (\bullet) reactions at 873 K^a on 0.2% wt. Pt/Al₂O₃ (8.5 nm mean cluster diameter). (1 kPa C_2H_6 ; 1 kPa C_2D_6 ; 4.9 kPa CH_4 ; reaction conditions as described in Fig. 3a and b ^adata from [9].)

reactions that are 23 ± 4 times larger than O_2/CH_4 ratios in CH_4-O_2 reactions at the same O^* coverage:

$$\frac{(O_2)}{(C_2H_6)} \Big|_{O^*} = (23 \pm 4) \frac{(O_2)}{(CH_4)} \Big|_{O^*} \quad (16)$$

as shown by the O_2/C_nH_{2n+2} ratios at the transition from O^* to $*$ as MASI, which lead to the coincidence of this maximum rate for CH_4 and C_2H_6 reactants when the abscissa scales in Fig. 3a and b are corrected by the numerical coefficient shown in Eq. (16).

Thus, at each O^* coverage in regime 2, set by O_2/C_2H_6 ratios that are offset by a factor of 23 ± 4 from O_2/CH_4 ratios (Eq. (16), 773 K), pseudo-first-order rate constants for C_2H_6 are ~ 15 times larger than for CH_4 (Fig. 3a and b). Pseudo-first-order rate constants for CH_4-O_2 and $C_2H_6-O_2$ reactions on Pt are given by Eq. (5) (Section 3.4), which gives the following expression for the first-order rate constant for CH_4-O_2 reactions in regime 2:

$$\frac{r_{CH_4}}{(CH_4)} \Big|_{O^*} = \left(\frac{4}{2}\right) \frac{k_{1,2-C1H}^2}{K_{2a}k_{2bf}} \left(\frac{(O_2)}{(CH_4)} \Big|_{O^*}\right)^{-1} \quad (17a)$$

At the same O^* coverages as those set by O_2/CH_4 ratios in CH_4-O_2 reactions, the pseudo-first-order rate constants for $C_2H_6-O_2$

reactions in regime 2 are set by the O_2/C_2H_6 ratios and thus by the O_2/CH_4 ratios via Eq. (15):

$$\frac{r_{C_2H_6}}{(C_2H_6)} \Big|_{O^*} = \left(\frac{7}{2}\right) \frac{k_{1,2-C2H}^2}{K_{2a}k_{2bf}} \left(\frac{7}{4}\right) \frac{k_{1,2-C2H} (O_2)}{k_{1,2-C1H} (CH_4)} \Big|_{O^*}^{-1} \quad (17b)$$

Combining Eqs. (17a) and (17b) leads to pseudo-first-order rate constants for C_2H_6 that are higher than those for CH_4 at equivalent O^* coverages by a constant factor given by the rate constant ratio for the respective C–H bond activation elementary steps:

$$\frac{r_{C_2H_6}}{(C_2H_6)} \Big|_{O^*} = \frac{k_{1,2-C2H}}{k_{1,2-C1H}} \frac{r_{CH_4}}{(CH_4)} \Big|_{O^*} \quad (18)$$

The rate constant ratio ($k_{1,2-C2H}/k_{1,2-C1H}$) on Pt (8.5 nm mean cluster size) at 773 K is equal to 13 ± 2 (Table 2; Supplementary information, Section S5) and corresponds to the difference in pseudo-first-order rate constants at equal O^* coverage, reflected in the difference between the ordinate scales shown in Fig. 3a and b.

Rate constants for C_2H_6 and CH_4 oxidation in regime 3 ($O_2/C_2H_6 = 0-0.7$; $O_2/CH_4 = 0-0.03$; Section 3.5) do not depend on the concentration or the identity of the alkane reactant (Figs. 3a and 6), because O_2 dissociation on nearly bare Pt clusters becomes the sole kinetically-relevant step. First-order rate constants for C_2H_6 and CH_4 reactions at a given O_2/C_nH_{2n+2} ratio in regime 3 are related to each other by their respective O_2 consumption stoichiometries ($(3n+1)/2$, Eqs. (12) and (13)):

$$\frac{r_{C_2H_6}}{(C_2H_6)} = \left(\frac{2}{7}\right) \frac{K_{2a}k_{2bf}}{K_{2a}k_{2bf}} \frac{r_{CH_4}}{(CH_4)} = \left(\frac{2}{7}\right) \frac{r_{CH_4}}{(CH_4)} \quad (19)$$

which equals the ratio of the measured pseudo-first-order rate constants (0.57 ± 0.02 ; 0.2% wt. Pt/Al₂O₃; 8.5 nm clusters; 773 K; Table 2).

These mechanistic connections between CH_4-O_2 and $C_2H_6-O_2$ reactions allow us to infer turnover rates and O^* coverages based on C–H bond reactivity and energies. Weaker C–H bond in C_2H_6 lead to higher rates than for CH_4 when C–H bond activation on O^*-O^* or O^*-* site pairs is the kinetically-relevant step (regimes 1 and 2); activation energies decrease as C–H bonds become weaker with increasing chain size, but also because stabilization of the alkyl group via interactions with O^* at the transition state becomes more effective for larger alkyls. When Pt surfaces are bare and the C–H bond activation is no longer the kinetically-relevant step (regime 3), O_2 dissociation limits rates and differences between alkanes solely reflect their respective stoichiometric O_2 requirements.

3.7. Effects of Pt coordination number and O^* binding strength on $C_2H_6-O_2$ turnover rates

Coordinationally unsaturated corner and edge atoms become more prevalent as Pt clusters become smaller [36] and the binding energies of O^* and other chemisorbed species concurrently increase. The higher O^* binding energies on low-coordination atoms are consistent with stepped Pt(112) surfaces that desorb O^* at higher temperatures than low-index Pt(111) surfaces [37]. These effects of coordination are expected to lead to marked effects of Pt cluster size effects on O^* binding and reactivity and on the availability of vacant sites during steady-state alkane oxidation catalysis. Oxygen binding energy influences its reactivity for H abstraction in regimes 1 and 2, while the number of vacancies during steady-state catalysis determines the number of O^*-* sites available for C–H bond activation in regime 2. These considerations lead us to conclude that turnover rates will depend on Pt cluster size for $C_2H_6-O_2$ reactions, as recently shown also for CH_4-O_2 reactions on Pt [11] and Pd [13] clusters; specifically,

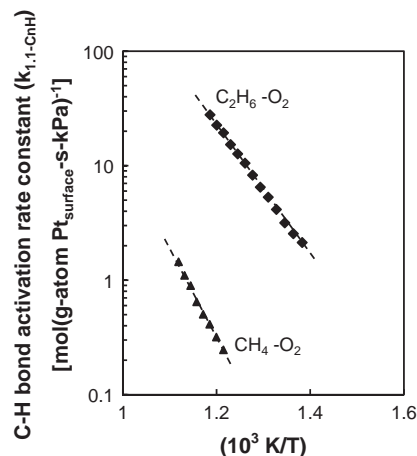


Fig. 7. Arrhenius plot of C–H bond activation rate constants on O^*-O^* site pairs ($k_{1,1-CnH}$; regime 1) on O^* -saturated Pt clusters during CH_4-O_2 (\blacktriangle , $k_{1,1-C1H}$) and $C_2H_6-O_2$ (\blacksquare , $k_{1,1-C2H}$) reactions. (Reaction conditions as described in Fig. 3a and b; ^adata from [9].)

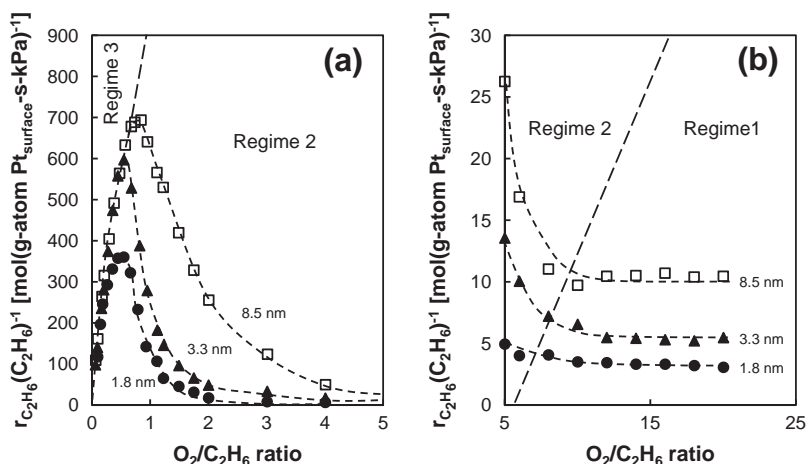


Fig. 8. (a and b) Pseudo-first-order rate constants ($r_{\text{C}_2\text{H}_6}(\text{C}_2\text{H}_6)^{-1}$) as a function of $\text{O}_2/\text{C}_2\text{H}_6$ ratio, in the range of (a) 0–5 and (b) 5–20 $\text{O}_2/\text{C}_2\text{H}_6$ ratios, on 0.2% wt. Pt/ Al_2O_3 catalysts with mean Pt cluster size diameters of 1.8 nm (●), 3.3 nm (▲), and 8.5 nm (□). (1 kPa of C_2H_6 ; reaction conditions as described in Fig. 3a and b.)

smaller Pt clusters are expected to show lower turnover rates in the range of cluster sizes (1.8–8.5 nm) that cause concomitant changes in the average coordination of exposed Pt atoms, as found experimentally and shown by the turnover rate data for kinetic regimes 1 and 2 in Fig. 8a and b.

In regime 1, pseudo-first-order rate constants ($r_{\text{C}_2\text{H}_6}(\text{C}_2\text{H}_6)^{-1}$, Fig. 8b) reflect those for C–H bond activation elementary steps on O^*-O^* site pairs ($k_{1,1-\text{C}_2\text{H}_6}$, Table 4); their values increased with increasing Pt cluster size, as the fraction of exposed atoms located at low-index planes concurrently increased. More weakly-bound O^* atoms at low-index planes are more reactive in C–H bond activation than O^* species at the coordinatively-unsaturated edge and corner sites that prevail on smaller clusters, as shown from cluster size effects on CH_4-O_2 turnover rates on Pt [11] and Pd [13] when O^*-O^* sites activate C–H bonds and on dimethyl ether combustion on Pt [38]. Weakly-bound O^* at low-index terraces bind H more strongly than O^* atoms at corners and edges and lead to smaller C–H bond activation barriers than on corners and edges, as shown also by DFT-derived C–H bond activation barriers on O^*-O^* site pairs on Pt_{201} clusters (149 kJ mol^{-1} on terrace sites vs. 170–175 kJ mol^{-1} for corners and edges) [11].

In regime 2, pseudo-first-order rate constants ($r_{\text{C}_2\text{H}_6}(\text{C}_2\text{H}_6)^{-1}$, Fig. 8a and b) increase with increasing Pt cluster size. These rate constants reflect the combined effects of those for C–H bond activation on O^*-O^* site pairs and for O_2 dissociation on $^*-\text{O}^*$ pairs ($3.5k_{1,2-\text{C}_2\text{H}_6}^2/(K_{2a}k_{2\text{br}})^{-1}$, Table 4). In this regime, C–H bond activation requires vacancies to stabilize the C-atom in the alkyl group at the transition state [11] (Section 3.4); therefore, the effects of Pt coordination on rate constants depend not only on O^* reactivity, as in the case of regime 1, but also on the strength of C–Pt interactions

Table 4

Effects of mean Pt cluster diameter on effective rate constants during $\text{C}_2\text{H}_6-\text{O}_2$ reactions on Pt/ Al_2O_3 catalysts at 773 K.

Mean Pt cluster diameter (nm)	Effective rate constants ^a ($\text{mol C}_2\text{H}_6 (\text{g-atom Pt}_{\text{surface-S-kPa}})^{-1}$)		
	Regime 1 $k_{1,1-\text{C}_2\text{H}_6}$	Regime 2 $\left(\frac{3.5 k_{1,2-\text{C}_2\text{H}_6}^2}{K_{2a} k_{2\text{br}}}\right)^{-1}$	Regime 3 $\left(\frac{K_{2a} k_{2\text{br}}}{3.5}\right)^{-1}$
1.8	3.3 ± 0.1	200 ± 20	1400 ± 100
3.3	5.3 ± 0.2	370 ± 30	1510 ± 50
8.5	9.6 ± 0.7	710 ± 30	1590 ± 20

Interparticle quartz/catalyst ratio (χ) of 7000; $6.01 \times 10^7 \text{ cm}^3 (\text{STP}) \text{ g}^{-1} \text{ h}^{-1}$.

^a $k_{\text{eff},\text{C}_2\text{H}_6}$, defined in Table 2; 0.2% wt. Pt/ Al_2O_3 ; intraparticle $\text{SiO}_2/\text{catalyst}$ ratio (λ) of 300;

at exposed metal atom and on the fraction of cluster surfaces uncovered by O^* . On large clusters, C–Pt interactions are weaker, leading to less-stable transition states, as shown from DFT-derived metal– CH_3 bond energies and C–H bond activation barriers on Pt clusters [12]. Larger clusters, however, also bind O^* more weakly, leading to more reactive oxygen atoms and to higher vacancy densities. As in the case of regime 1, weakly-held O^* species prevalent on large clusters are better H abstractors and lead to lower C–H bond activation barriers [11].

In regime 3, pseudo-first-order rate constants ($r_{\text{C}_2\text{H}_6}(\text{C}_2\text{H}_6)^{-1}$, Fig. 8a) reflect those for O_2 dissociation elementary steps ($K_{2a}k_{2\text{br}}/3.5$, Table 4) and are essentially independent of Pt cluster size, in contrast with the strong catalytic consequences of size in regimes 1 and 2. O_2 dissociation rates are unaffected by the coordination of exposed atoms, consistent with the barrierless and highly exothermic nature of these elementary steps, which are mediated by very early transition states that do not sense the stability or the binding energy of the final O^* species formed as the final products of O_2 dissociation steps.

Fig. 9a and b show the effective rate constants for $\text{C}_2\text{H}_6-\text{O}_2$ reactions in each kinetic regime as a function of mean Pt cluster size, together with those for CH_4-O_2 (873 K, [11]) reactions. The effects of cluster size and O^* binding energy are similar for C_2H_6 and CH_4 [11] in each kinetic regime, consistent with the rigorous mechanistic analogies between C_2H_6 and CH_4 reactions with O_2 . Rate constants increase with increasing cluster size in those kinetic regimes for which C–H bond activation is the kinetically-relevant step (on O^*-O^* or O^*-O^* site pairs; regimes 1 and 2); they become insensitive to cluster size and surface coordination when O_2 activation on bare cluster surfaces becomes the sole kinetically-relevant step (regime 3).

The elementary steps, kinetic regimes, and mechanistic analogies reported here for C_2H_6 and CH_4 reactions with O_2 are consistent with all rate data and kinetic isotope effects, with differences in C–H bond energies and in alkyl binding, and with the catalytic consequences of surface coordination and cluster size. These mechanistic connections among alkanes provide predictive guidance for the reactivity and rate equations for the combustion of larger alkanes (some additional discussion about the procedures required for estimating the kinetic behavior of larger alkanes is included in the Supplementary information, Section S6) and also for other metals while also resolving seemingly complex kinetic behavior in terms of a simple and chemically sound sequence of elementary steps.

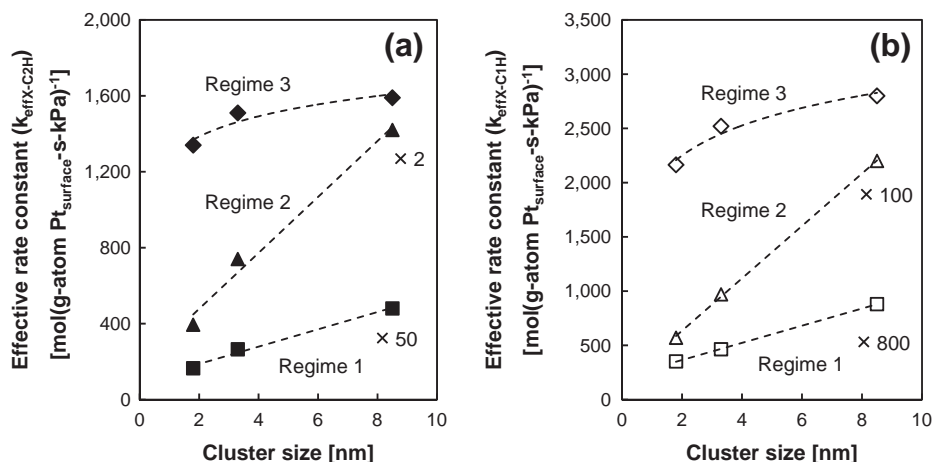


Fig. 9. (a and b) Effective rate constants ($k_{\text{eff}(X-C_{nH})}$, as defined in Table 2; X: regime 1, 2, or 3) on 0.2% wt. Pt/ Al_2O_3 catalysts as a function of mean Pt cluster size diameters during $\text{C}_2\text{H}_6\text{-O}_2$ ((a); (◆, ▲, ■)) and $\text{CH}_4\text{-O}_2$ ((b); (◇, △, □)) reactions in regime 1 (■, □), regime 2 (▲, △) and regime 3 (◆, ◇). ((a) 773 K, reaction conditions as described in Fig. 3a and b; (b) 873 K, data from [9].)

4. Conclusions

Kinetic and isotopic assessments of C_2H_6 oxidation on Pt clusters show that combustion products form almost exclusively via a sequence of elementary steps identical to those in CH_4 oxidation reactions. Both $\text{CH}_4\text{-O}_2$ and $\text{C}_2\text{H}_6\text{-O}_2$ reactions exhibit three equivalent kinetic regimes that evolve with changes in chemisorbed oxygen (O^*) coverages. Each of these regimes possesses distinct rate equations, kinetic isotope effects, and cluster size effects, which reflect changes in the kinetically-relevant steps and most abundant surface intermediates (MASI). However, the turnover rates for alkane conversion and the $\text{O}_2/\text{C}_n\text{H}_{2n+2}$ ratios required for transition among kinetic regimes are different between CH_4 and C_2H_6 because of their differences in C–H bond strength, O_2 consumption stoichiometry, and extent to which the alkyl group interacts with the chemisorbed O^* atoms at the transition states.

$\text{O}_2/\text{C}_n\text{H}_{2n+2}$ ratios that result in oxygen-saturated Pt surfaces (regime 1) lead to rates that are first-order in reductant (CH_4 or C_2H_6) pressure and independent of O_2 pressure; C–H bond activation on $\text{O}^*\text{-O}^*$ site pairs is the kinetically-relevant step and involves transition states with radical-like alkyls. Vacancy sites emerge as $\text{O}_2/\text{C}_n\text{H}_{2n+2}$ ratios decrease (regime 2), and C–H bonds are activated more effectively on $\text{O}^*\text{-}$ than on $\text{O}^*\text{-O}^*$ site pairs, because alkyl groups at the transition states are stabilized by vacancy sites (*). When C–H bond activation is kinetically-relevant, turnover rates increase with alkane chain size because of the concomitant decrease in C–H bond strength and because larger alkyl groups are more effectively stabilized via van der Waals interactions with the surface and incipient coordination of alkyl species to O^* at the transition states. Vacancy sites, determined by the kinetic coupling of C–H and $\text{O}=\text{O}$ activation steps, emerge at higher $\text{O}_2/\text{C}_n\text{H}_{2n+2}$ ratios for C_2H_6 than for CH_4 due to greater rates of O^* scavenging resulting from the higher C–H bond reactivity in C_2H_6 . Turnover rates increase with increasing cluster size in regimes 1 and 2 because weakly-bound O^* species, prevalent on large Pt clusters, are more effective in abstracting the H than more tightly bound O^* species on small Pt clusters. As the $\text{O}_2/\text{C}_n\text{H}_{2n+2}$ ratios decrease further, Pt clusters become bare (regime 3) and C–H bond activation is no longer kinetically-relevant, and therefore, turnover rates are independent of the concentration and identity of the reductant. Rates on these uncovered surfaces are limited by non-activated O_2 dissociation steps and thus are independent of the cluster size.

Together, these data provide mechanistic analogies between $\text{CH}_4\text{-O}_2$ and $\text{C}_2\text{H}_6\text{-O}_2$ reactions and predictive relations for the rate dependencies on O_2 and reductant pressures in each kinetic regime. The mechanistic similarities between CH_4 and C_2H_6 oxidation paths, in which the kinetic dependencies are direct consequences of O^* coverages and C–H bond reactivity, imply that these elementary steps and the kinetic consequences of O^* coverage can be used as guidance for the prediction of reaction pathways, kinetic parameters, and transitions among kinetic regimes for the oxidation of larger alkanes.

Acknowledgments

This study has been funded by BP as part of the Methane Conversion Cooperative Research Program at the University of California at Berkeley. We thank Professor Matthew Neurock and Dr. Corneliu Buda (University of Virginia) for helpful technical discussions and for their collaboration and contributions to the CH_4 part of this work, the details of which have been published elsewhere.

Appendix A. Supplementary material

Supplementary data associated with this article can be found, in the online version, at doi:10.1016/j.jcat.2011.09.036.

References

- [1] J.G. McCarty, Catal. Today 26 (1995) 283.
- [2] M. Prettre, C. Eichner, M. Perrin, Trans. Faraday Soc. 42 (1946) 335.
- [3] J.R. Rostrup-Nielsen, Catal. Today 71 (2002) 243.
- [4] Aisling M. O'Connor, Julian R.H. Ross, Catal. Today 46 (1998) 203.
- [5] A.T. Ashcroft, A.K. Cheetham, J.S. Foord, M.L.H. Green, C.P. Grey, A. J Murrell, P.D.F. Vernon, Nature 344 (1990) 319.
- [6] T.F. Garetto, C.R. Apesteguía, Catal. Today 62 (2000) 189.
- [7] S. Liu, G. Xiong, W. Yang, L. Xu, G. Xiong, C. Li, Catal. Lett. 63 (1999) 167.
- [8] H. Wang, Y. Cong, W. Yang, J. Membr. Sci. 209 (2002) 143.
- [9] N. Iwasaki, T. Miyake, E. Yagasaki, T. Suzuki, Catal. Today 111 (2006) 391.
- [10] M. Huff, P.M. Tornaiainen, L.D. Schmidt, Catal. Today 21 (1994) 113.
- [11] Y.H. Chin, C. Buda, M. Neurock, E. Iglesia, J. Am. Chem. Soc. 133 (2011) 15958.
- [12] Y.H. Chin, C. Buda, M. Neurock, E. Iglesia, J. Catal. 283 (2011) 10.
- [13] Y. H. Chin, E. Iglesia, submitted J. Phys. Chem. C 115 (2011) 17845.
- [14] M.A. Bañares, Catal. Today 51 (1999) 319.
- [15] V.D. Sokolovskii, Catal. Today 24 (1995) 377.
- [16] W.M. Haynes, Thermodynamic Properties as a Function of Temperature in CRC Handbook of Chemistry and Physics, 91st ed., CRC Press/Taylor and Francis, Boca Raton, FL, 1991 (Internet Version 2011).
- [17] A. Yamaguchi, E. Iglesia, J. Catal. 274 (2010) 52.
- [18] J. Wei, E. Iglesia, J. Catal. 225 (2004) 116.

- [19] W.M. Haynes, Physical Constants of Inorganic Compounds in CRC Handbook of Chemistry and Physics, 91st Ed., CRC Press/Taylor and Francis, Boca Raton, FL, 1991 (Internet Version 2011).
- [20] R.M. Koros, E.J. Nowak, Chem. Eng. Sci. 22 (1967) 470.
- [21] R. Madon, M. Boudart, Ind. Eng. Chem. Fundam. 21 (1982) 438.
- [22] J. Wei, E. Iglesia, J. Phys. Chem. B 108 (2004) 4094.
- [23] B.M. Weiss, E. Iglesia, J. Phys. Chem. C 113 (2009) 13331.
- [24] T. Li, P.B. Balbuena, J. Phys. Chem. B 105 (2001) 9943.
- [25] F.H. Westheimer, Chem. Rev. 61 (1961) 265.
- [26] T. Shimanouchi, Tables of Molecular Vibrational Frequencies Consolidated, vol. I, NSRDS-NBS 39, Washington, DC, 1972.
- [27] K.B. Wiberg, J.J. Wendoloski, J. Phys. Chem. 88 (1984) 586.
- [28] H.P. Bonzel, R. Ku, Surf. Sci. 40 (1973) 85.
- [29] D.R. Monroe, R.P. Merrill, J. Catal. 65 (1980) 461.
- [30] Y.H. Chin, C. Buda, M. Neurock, E. Iglesia, in preparation
- [31] Stephen J. Blanksby, G. Barney Ellison, Acc. Chem. Res. 36 (2003) 255.
- [32] B.A. Sexton, A.E. Hughes, Surf. Sci. 140 (1984) 227.
- [33] D.R. Mullins, S.D. Senanayake, T.-L. Chen, J. Phys. Chem. C 114 (2010) 17112.
- [34] M.K. Welden, C. Friend, Chem. Rev. 96 (1996) 1391.
- [35] G. Glockler, J. Phys. Chem. 62 (1958) 1049.
- [36] R. Van Hardeveld, F. Hartog, Surf. Sci. 15 (1969) 189.
- [37] A. Winkler, X. Guo, H.R. Siddiqui, P.L. Hagans, J.T. Yates Jr., Surf. Sci. 201 (1988) 419.
- [38] A. Ishikawa, M. Neurock, E. Iglesia, J. Am. Chem. Soc. 129 (2007) 13201.